Sustainable Energy & Fuels

ROYAL SOCIETY OF CHEMISTRY

PAPER

View Article Online
View Journal | View Issue

Cite this: *Sustainable Energy Fuels*, 2025, **9**, 4364

A layered double hydroxides/MXene composite based triboelectric nanogenerator for energy harvesting and self-powered electroplating applications†

Navaneeth Madathil,[a] Anjaly Babu,[a] Mahesh Velupula,[a] Anu Kulandaivel,[a] Rakesh Kumar Rajaboina, *[a] Uday Kumar Khanapuram, *[a] Kamakshaiah Charyulu Devarayapalli [b] and Dae Sung Lee *[b]

The increasing demand for sustainable energy solutions has spurred research into advanced energy-harvesting technologies, with triboelectric nanogenerators (TENGs) emerging as a promising option for converting ambient mechanical energy into electrical power. The present study explores the potential of a novel composite material comprising nickel–aluminum layered double hydroxides (NiAl-LDH) and MXene (Ti_3C_2) to improve TENG performance. Integrating highly conductive, high-surface-area two-dimensional (2D) MXenes with multifunctional 2D layered double hydroxides (LDHs) leverages their synergistic properties to enhance charge generation and transfer efficiency, achieving an impressive power density of 36.9 W m^{-2}, the highest reported for LDH-based TENGs. In addition to advancing energy harvesting, the TENG device was utilized to design a self-powered electroplating system. Here, energy harvested by the TENG from mechanical motion was stabilized through a power management circuit and used to drive an electrochemical process, successfully coating copper onto metal objects. The presented work paves the way for eco-friendly, sustainable manufacturing, showcasing the potential of TENGs for powering small-scale electrochemical tasks without relying on external power supplies. The results of this study highlight the versatility and promise of NiAl-LDH/MXene-based TENGs for a wide range of energy-harvesting and industrial applications.

Received 8th April 2025
Accepted 26th June 2025

DOI: 10.1039/d5se00492f

rsc.li/sustainable-energy

1 Introduction

The growing demand for sustainable energy solutions has accelerated research into advanced energy-harvesting technologies that convert ambient energy into usable electrical power. Among the most promising of these technologies are triboelectric nanogenerators (TENGs), which harness mechanical energy from environmental sources, such as human movement, vibrations, and wind, and convert it into electricity.[1–3] TENGs operate based on the principles of triboelectrification and electrostatic induction.[4,5] When two materials with differing triboelectric polarities come into contact and are subsequently separated, electrical energy is generated, which can be harvested and stored. This mechanism has garnered significant interest due to its simplicity, scalability, vast material choices, and potential applications in self-powered electronics, sensors, and renewable energy systems.[6–9]

A wide range of materials have been explored for TENG fabrication to enhance their energy output, efficiency, and durability. The materials used in TENGs span a diverse spectrum, including polymers,[10,11] metal oxides,[12,13] organic materials,[14,15] waste by-products,[16,17] metals,[18,19] 2D materials,[20,21] porous materials[22,23] *etc.* Each material class contributes specific properties that affect the triboelectric effect, the charge generation process, and the device's overall performance. Polymers, for example, are lightweight and flexible, making them ideal candidates for wearable TENGs, while metal oxides offer robust mechanical strength and chemical stability, enabling durable energy-harvesting devices.

This study investigates a relatively unexplored class of materials in the TENG field: layered double hydroxides (LDHs), particularly those based on nickel and aluminum (NiAl-LDH). LDHs are a family of two-dimensional materials characterized by a structure similar to brucite $Mg(OH)_2$, where some divalent metal cations (M^{2+}) are partially substituted by trivalent metal cations (M^{3+}). This substitution creates an excess positive charge, which is balanced by intercalated anions in the

[a]*Department of Physics, Energy Materials and Devices (EMD) Lab, National Institute of Technology, Warangal-506004, India. E-mail: rakeshr@nitw.ac.in; kanapuram.udaykumar@nitw.ac.in*

[b]*Department of Environmental Engineering, Kyungpook National University, Buk-gu, Daegu 41566, Republic of Korea. E-mail: daesung@knu.ac.kr*

† Electronic supplementary information (ESI) available. See DOI: https://doi.org/10.1039/d5se00492f

interlayer spaces, along with water molecules. LDHs are represented by the general formula $[M_{1-x}^{2+}\ M_x^{3+}(OH)_2]^{x+}\ [A^{n-}]_{x/n}\cdot mH_2O$, where M represents divalent/trivalent heterogeneous metal cations (Ni^{2+} and Al^{3+}), and A represents anions (NO_3^-). The versatility of LDHs lies in their tunable chemical composition, high surface area, and potential for functionalization, which make them suitable for applications in catalysis, drug delivery, and, more recently, energy storage and conversion technologies.[24–26] LDHs can serve as an effective triboelectric positive layer in TENGs due to their intrinsic positive charge, arising from the partial substitution of M^{2+} with M^{3+}, which enhances their ability to donate electrons during contact electrification.

MXenes, a class of two-dimensional transition metal carbides and nitrides, have become a focal point in recent research due to their excellent electrical conductivity, hydrophilicity, and surface functionality. Their unique properties make them ideal for integration into TENGs as conductive layers or frictional layers or in combination with other materials to enhance charge generation and transfer.[27,28] MXenes have been extensively studied for their role in energy storage, capacitors, and electromagnetic shielding, while their use in TENGs has only recently gained attention.[29–31]

The heterostructure formed by growing LDH on MXene sheets effectively prevents the agglomeration and restacking of both NiAl-LDH and MXene. The interfacial electronic coupling in MXene/LDH heterostructures enhances conductivity, increases active sites, and improves stability. MXene, when combined with a semiconductor like LDH, forms an interfacial Schottky junction, facilitating efficient charge carrier separation and migration.[32] The combination of MXene with NiAl-LDH in a TENG device offers an innovative approach to improving the power output of triboelectric systems. This study represents one of the first comprehensive explorations of NiAl-LDH/MXene composites in TENG applications, with the goal of filling a critical gap in the literature on the use of LDHs for energy harvesting. This composite material leverages the unique properties of both components: the high surface area and tuneable chemistry of NiAl-LDH, combined with the exceptional electrical conductivity and surface functionality of MXenes. MXenes, due to their two-dimensional structure, have the ability to facilitate rapid charge transfer and enhance the electrostatic interactions between triboelectric layers. This makes them ideal for pairing with LDHs, which are electron-donating materials. The synergy between NiAl-LDH and MXenes could lead to improved triboelectric performance by increasing the surface charge density, optimizing charge transfer efficiency, and enhancing the device's overall durability. A comprehensive review of LDH and MXene-based TENGs is presented in ESI-S1,† highlighting the novelty and superior performance of our NiAl-LDH/MXene-based TENG in comparison to previously reported systems.

In our experiments, we utilized a NiAl-LDH/MXene composite as the positive triboelectric layer, while fluorinated ethylene propylene (FEP) was employed as the negative triboelectric layer. FEP is a widely used material in TENGs due to its strong electron-accepting properties and high durability. The combination of NiAl-LDH/MXene as the electron-donating layer and FEP as the electron-accepting layer creates an optimal triboelectric pairing. The device demonstrated impressive performance metrics, producing an open-circuit voltage (V_{oc}) of 734 V and a short-circuit current (I_{sc}) of 355 μA. These values are notably high for a TENG based on LDH materials, indicating that the NiAl-LDH/MXene composite significantly enhances the triboelectric effect. At an optimized load resistance of 2 MΩ, the power density of the device reached 36.9 W m^{-2}. This value represents the highest reported power density for a TENG incorporating an LDH-based material, underscoring the potential of this composite for high-efficiency energy harvesting applications.

Further, we have demonstrated great potential for powering small-scale electrochemical processes, including the design of self-powered electroplating systems. This self-powered electroplating setup demonstrates the feasibility of using energy harvested from ambient mechanical sources to perform electrochemical tasks without relying on external power supplies, paving the way for eco-friendly and sustainable manufacturing techniques.

2 Experimental section

2.1 Preparation of multi-layered MXene (Ti_3C_2)

The 2D MXene nanosheets were synthesized using selective aluminum etching from the parental MAX phase followed by delamination *via* probe sonication, similar to what has been reported in the literature.[33] The schematic of the synthesis procedure is presented in Fig. 1(a). The parent MAX phase Titanium aluminum carbide (Ti_3AlC_2) was purchased from Sigma Aldrich and used directly without further purification. 1 g of Ti_3AlC_2 was added to 20 mL of Hydrofluoric acid (HF) (48 wt%) and magnetically stirred for 24 h at 250 rpm. Multi-layered MXene was obtained after centrifuging (3500 rpm), and washed several times with deionised (DI) water until it reached a neutral pH of 6–7.

2.2 Delamination of multi-layered MXene (Ti_3C_2)

The MXene powder, consisting of multiple layers, was mixed with Dimethyl sulfoxide (DMSO, 99.5 wt%) at a ratio of 1 : 15 (g) and stirred at 400 rpm for 18 hours. After dilution with water, the DMSO-intercalated MXene was collected by centrifugation at 3500 rpm for 25 minutes. The resulting MXene powder was dispersed in DI water at 1 : 300 and sonicated for 6 hours (750 W, 20 kHz). The supernatant was obtained by centrifuging at 3500 rpm for 1 hour. Few-layered MXene nanosheets were acquired through vacuum filtration of the supernatant, followed by vacuum drying.[34] A photograph of the obtained MXene nanosheet powder is shown in Fig. 1(b). The morphology and crystallinity of the obtained powder were characterized using Field Emission Scanning Electron Microscopy (FESEM, Model JSM-IT 800) and X-ray Diffraction (XRD, XRD dynamics 500).

2.3 Preparation of NiAl-LDH and the NiAl-LDH/MXene composite

Fig. 1(c) illustrates the schematic representation of the synthesis process for the NiAl-LDH/MXene composite. A

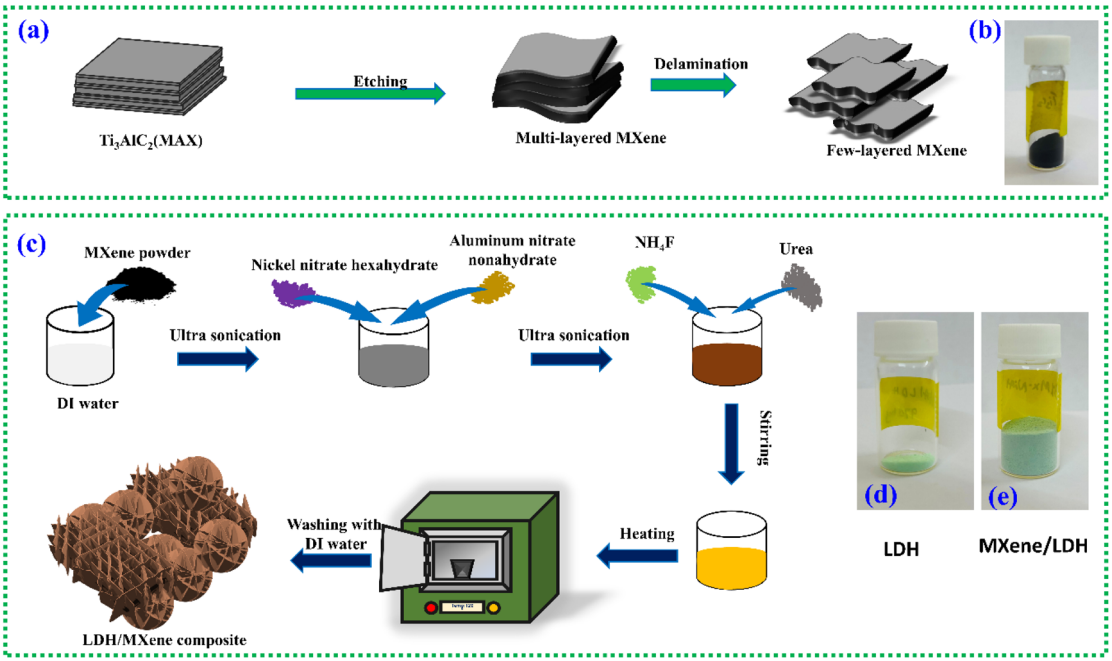

Fig. 1 (a) Schematic illustration of the MXene powder synthesis, (b) photograph of the MXene powder, (c) schematic representation of the synthesis procedure for the NiAl-LDH/MXene nanocomposite, (d) photograph of the LDH powder, (e) photograph of the MXene/LDH powder.

specific quantity of MXene nanosheet powder was dispersed in DI water using ultrasonic treatment. 0.002 M aluminum nitrate nonahydrate ($Al(NO_3)_3 \cdot 9H_2O$) and 0.006 M nickel nitrate hexahydrate ($Ni(NO_3)_2 \cdot 6H_2O$) were added to the suspension followed by an additional 10 minutes of ultrasonication. Next, 0.04 M urea ($CO(NH_2)_2$) and 0.016 M ammonium fluoride (NH_4F) were mixed with the suspension and stirred for 30 minutes. The resulting suspension was then subjected to heat treatment at 120 °C for 24 hours. Finally, the obtained material was thoroughly washed with DI water until a neutral pH was achieved and then dried overnight at 80 °C. A series of LDH/MXene composites were synthesized by changing the weight percentage of MXene in LDH, *i.e.*,1, 2, and 3 wt%. Pure LDH was also synthesized by a similar procedure, but in the absence of MXene.[35] The photographs of the pure LDH and LDH/MXene composite powders are shown in Fig. 1(d) and (e), respectively.

2.4 Fabrication of a triboelectric layer using the NiAl-LDH/MXene nanocomposite

The NiAl-LDH/MXene powder was coated onto an aluminum electrode using conductive carbon tape to ensure good adhesion and conductivity. The aluminum electrode was precisely cut into 5.5 × 5.5 cm^2 sheets, and a layer of conductive carbon tape, which is adhesive on both sides, was attached to its surface. This sticky surface enabled a stable attachment of the NiAl-LDH/MXene powder. The powder was then carefully loaded onto the prepared surface and uniformly spread using a fine brush to ensure an even coating. This method ensured consistent material distribution, which is crucial for optimizing the device's triboelectric performance. The real-time photographs of the fabrication process are presented in ESI Fig. S2.†

2.5 TENG device fabrication and testing

The TENGs were constructed using a NiAl-LDH/MXene nanocomposite film as the fixed triboelectric layer, while the second frictional layer was attached to a separate aluminum electrode using conductive carbon tape. To evaluate the performance of the TENG, electrical connections were made between the top and bottom aluminum electrodes using two wires, and the device was tested in vertical contact separation (VCS) mode by applying a hand-tapping force of approximately 8–10 N (ESI S3†), and frequency of 4–5 Hz. Several triboelectric materials—including Kapton, poly(tetrafluoroethylene) (PTFE), FEP, silicone rubber, and poly(methyl methacrylate) (PMMA)—were tested against the NiAl-LDH/MXene nanocomposite to identify the combination yielding the best output. The electrical performance of the TENG was measured using an oscilloscope (GW-Instek, GDS-1102B) and a current preamplifier (SRS, SR570). The long-term stability and durability of the device were assessed using a custom-built tapping machine.

3 Results and discussion

3.1 Material characterization

The surface morphology of the synthesized nanocomposites was examined using FESEM. Fig. 2 presents the FESEM images of NiAl-LDH, MXene, and the NiAl-LDH/MXene composite at various magnifications. The pure NiAl-LDH displays a distinct 3D flower-like structure, as depicted in Fig. 2(a) and (b), which is consistent with previous reports in the literature.[36,37] In Fig. 2(c) and (d), the MXene exhibits its characteristic stacked, layered structure. Notably, Fig. 2(e) and (f) reveals that the NiAl-LDH is perfectly integrated on the MXene sheets. This structural

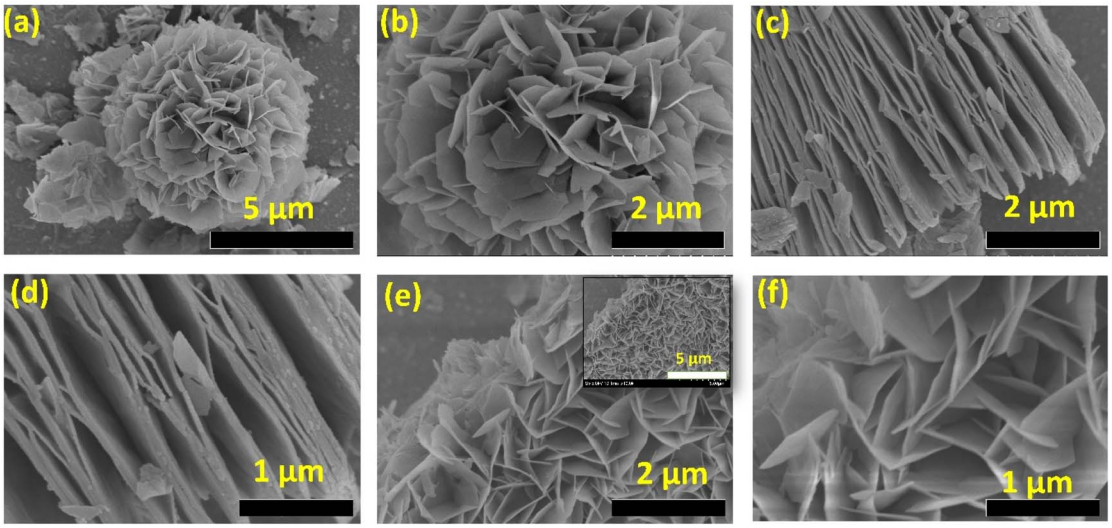

Fig. 2 FESEM images of (a) and (b) NiAl-LDH, (c) and (d) MXene, and (e) and (f) NiAl-LDH/MXene.

integration is crucial for enhancing the performance of the composite in energy harvesting applications. The uniformly distributed LDH on the conductive MXene substrate forms a well-integrated heterostructure, providing abundant active sites for contact electrification, which enhances charge transfer and boosts output performance.

To further validate the uniform distribution of LDH sheets on the MXene flakes, Energy Dispersive X-ray Analysis (EDAX) and elemental mapping were carried out, and the corresponding results are provided in ESI S4.† The elemental mapping reveals a consistent and well-dispersed presence of key elements such as nickel (Ni) and aluminum (Al), which are the primary constituents of the NiAl-LDH, across the entire surface of the MXene flakes. This uniform elemental distribution indicates that the LDH nanosheets have grown homogeneously on the MXene substrate without any significant agglomeration or localized deposition. The presence of titanium (Ti) and carbon (C), corresponding to the MXene structure, along with the even distribution of Ni and Al, further confirms the formation of a well-integrated hybrid structure.

The XPS spectra of the NiAl-LDH/MXene nanocomposite are shown in Fig. 3(a)–(d). The characteristic peaks of Ti, C, Ni, Al, O, and F elements at 457, 284, 855, 73, 530, and 683 eV, respectively, confirm the coexistence of NiAl-LDH and Ti_3C_2 in the nanocomposite. In the Ni_{2p} spectrum, the peaks at 855 eV and 873 eV correspond to the $2p_{3/2}$ and $2p_{1/2}$ doublet of Ni^{2+}, along with two shakeup satellites. The Al_{2p} spectrum shows a peak at 73 eV, indicating the presence of Al^{3+} in the composite. In the Ti_{2p} spectrum, the peaks at 463.6 eV and 457.8 eV are attributed to Ti–$O_{2p1/2}$ and Ti–$O_{2p3/2}$, respectively.[36,38]

The FTIR pattern of the NiAl-LDH/MXene composite is illustrated in Fig. 3(e). The peaks at 3560, 1634, and 1386 cm^{-1} correspond to the O–H stretching vibration of water molecules confined in the interlayer, hydrogen bonded OH groups, and N–O stretching vibrations from NO_3^-, respectively. Several peaks below 810 cm^{-1} can be attributed to M–O and M–O–M (M = Ni, Al) lattice vibrations.[39]

The XRD patterns of NiAl-LDH, MXene and the NiAl-LDH/MXene composite are illustrated in Fig. 3(f). The characteristic diffraction peaks of NiAl-LDH at 11.53°, 23.15°, 34.81°, 39.3°, 46.6°, 60.7°, and 62.03° correspond to the (003), (006), (012), (015), (018), (110) and (113) crystal planes respectively, which are well consistent with hexagonal phase (JCPDS No. 22-0452).[36,40,41] In the MXene/NiAl-LDH composite, the characteristic peak of NiAl-LDH is prominent, whereas the (002) diffraction peak of MXene is weaker and shifted to a smaller angle compared to exfoliated-MXene. This shift occurs because the NiAl-LDH nanosheets rest on the surface of MXene, preventing the restacking of MXene sheets. Additionally, the (002) peak of MXene is prone to overlap with signals from NiAl-LDH due to its low intensity.[42]

The Raman spectra of NiAl-LDH and NiAl-LDH/MXene are provided in ESI S5.† In the spectrum of NiAl-LDH, the characteristic peak observed at 1061 cm^{-1} can be ascribed to symmetric stretching mode of interlayer NO_3^-. In the spectrum of NiAl-LDH/MXene the two broad bands at 1354 and 1568 cm^{-1} are attributed to the D and G modes of carbon in MXene. The characteristic peaks of NiAl-LDH/MXene closely resemble those of NiAl-LDH due to the low MXene content in the composite, confirming the strong interaction between NiAl-LDH and MXene.[43]

3.2 Electrical characterization of the TENG

Fig. 4(a) shows the schematic of the TENG device with FEP and NiAl-LDH/MXene (2 wt%) layers as frictional layers. Fig. 4(b) illustrates the output performance of the fabricated TENG when the NiAl-LDH/MXene (2 wt%) composite layer was paired with various standard triboelectric materials. The experimental results show that the highest electrical output was achieved when the NiAl-LDH/MXene layer was paired with a FEP layer. This can be attributed to the strong electron-accepting properties of the FEP, which, in combination with the highly conductive and charge transfer enhancing qualities of the NiAl-LDH/MXene layer, maximized the triboelectric effect. Based on

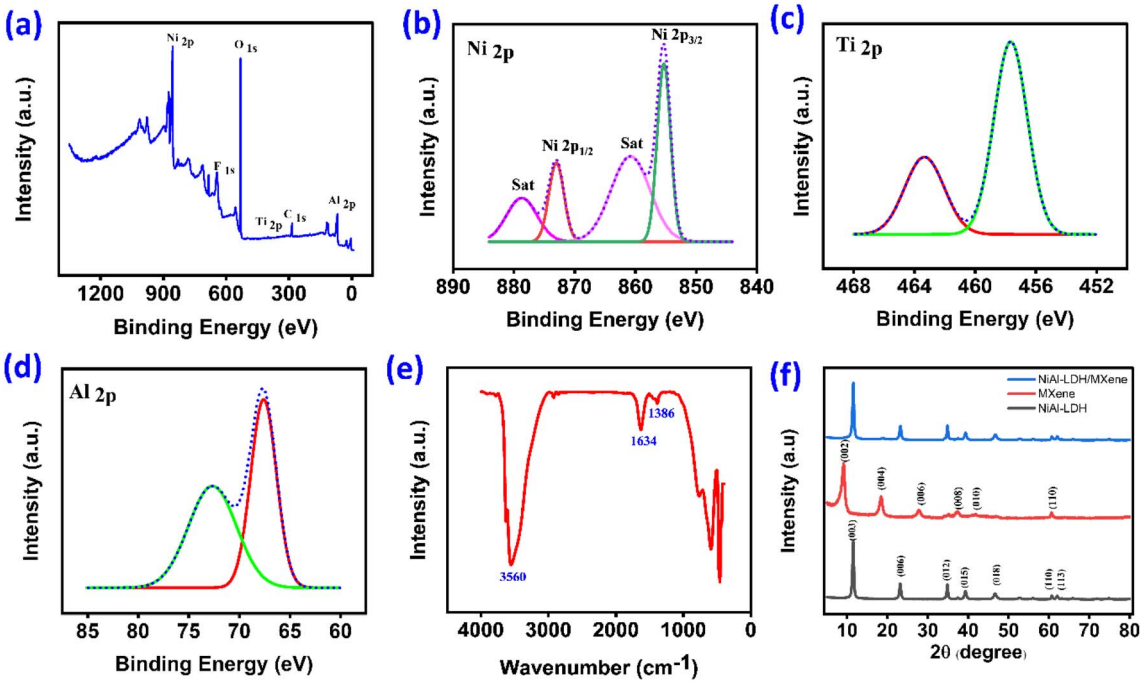

Fig. 3 XPS spectra of NiAl-LDH/MXene: (a) survey spectra, (b) Ni_{2p}, (c) Ti_{2p}, (d) Al_{2p}, (e) FT-IR spectra of the NiAl-LDH/MXene composite, (f) XRD pattern of MXene, NiAl-LDH and NiAl-LDH/MXene composite.

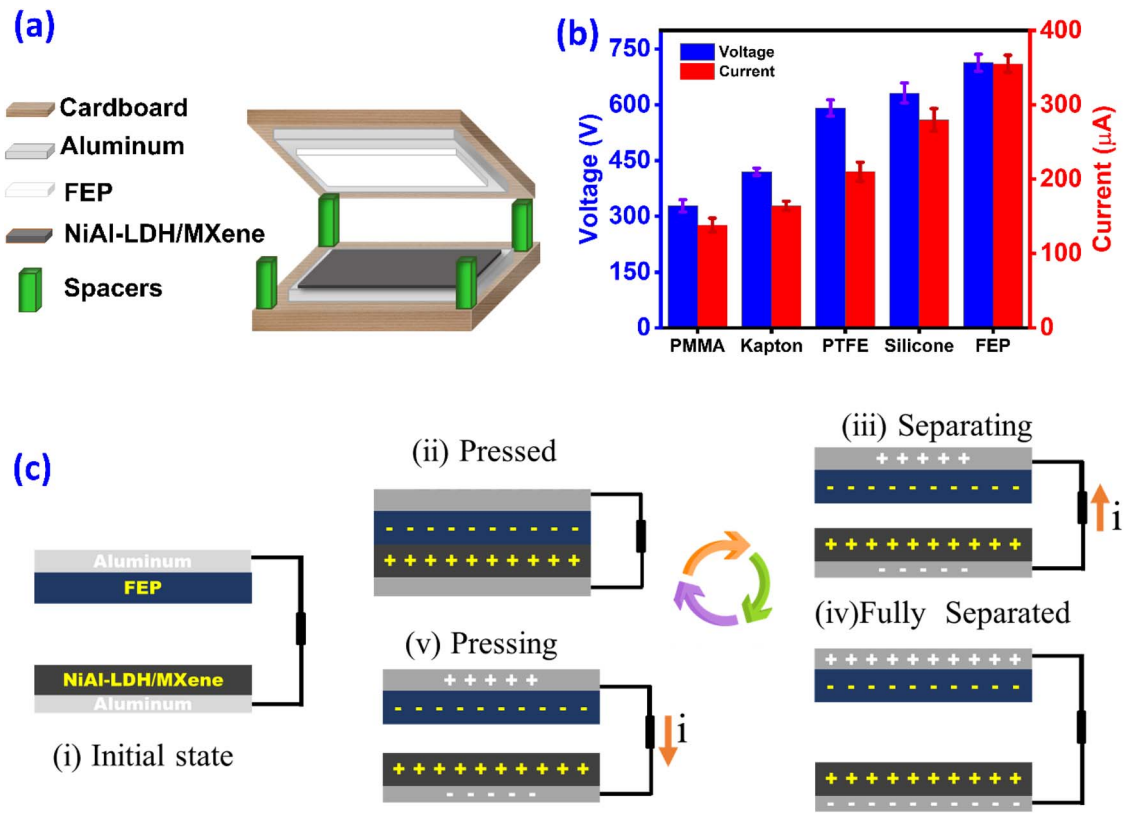

Fig. 4 (a) Schematic illustration of the fabricated TENG. (b) Output performance of the NiAl-LDH/MXene composite against different tribo-electric layers. (c) Schematic diagram of the working mechanism of the NiAl-LDH/MXene-TENG.

these results, the NiAl-LDH/MXene and FEP combination was chosen for further experiments due to its superior performance in generating electrical output.

Fig. 4(c) illustrates the current generation mechanism of the NiAl-LDH/MXene and FEP-based TENG. When a hand-tapping force is applied, the two frictional layers come into contact and exchange charges based on their electronegativity. As FEP is a strong electron acceptor, it gains electrons from the NiAl-LDH/MXene layer, leaving NiAl-LDH/MXene positively charged. After the applied tapping force is released, the frictional layers begin to separate, inducing a potential difference that drives electrons through the external circuit until equilibrium is reached. Reapplying the hand-tapping force brings the frictional layers closer together, causing electrons to flow in the reverse direction. This cyclic process of contact and separation generates an alternating current in the external circuit.

The detailed electrical characterization of the NiAl-LDH/MXene-FEP TENG is displayed in Fig. 5. The device reached maximum V_{oc} and I_{sc} values of 734 V and 355 μA, respectively, as shown in Fig. 5(a) and (b). The switching polarity test results confirm that the electrical output generated by the TENG device is not due to noise or external factors from the measuring instrument. Fig. 5(c) presents the variation in TENG output with different load resistance values, showing that the voltage rises while the current decreases as load resistance increases. Fig. 5(c) depicts a sharp increase in load voltage and a steep decrease in load current up to 20 MΩ, after which the values plateau as load resistance continues to increase. The instantaneous power density as a function of load resistance was calculated from the load characteristic data and illustrated in Fig. 5(d). The power density increased with load resistance, peaking at 36.9 W m^{-2} at a 2 MΩ load resistance, and then decreased as load resistance continued to rise. This variation in TENG power density can be explained using Ohm's law and maximum power transfer theorem, where the maximum power density is achieved when the load resistance matches the device's internal resistance.[44] The energy conversion efficiency of the TENG device was evaluated following a standard methodology reported in the literature (ESI S6†), and the TENG demonstrated an efficiency of approximately 85.05%, indicating effective conversion of mechanical energy into electrical energy. Furthermore, the stability of the TENG was evaluated over approximately 5200 cycles using an in-house-built linear tapping machine. The device maintained a stable output throughout the test, demonstrating its robustness and reliability. The reduced voltage observed in the stability test is due to the lower force exerted by the machine on the TENG compared to hand tapping. Further, the variation of output voltage and current as a function of hand tapping frequency has been systematically analyzed and is provided in ESI S7.† It can be observed that the output voltage and current initially increase with rising tapping frequency, reaching a maximum at around 4–5 Hz. However, when the frequency exceeded 5 Hz, both the output voltage and current began to decline. This trend is consistent with previously reported findings in the literature.[45,46]

To further optimize the TENG's performance, the MXene concentration in the NiAl-LDH/MXene composite was systematically varied at 0%, 1%, 2%, and 3%. The corresponding output voltage and current were measured (Fig. 6(a)) to assess the impact of MXene addition on device performance. When MXene was not incorporated (pure NiAl-LDH), the device

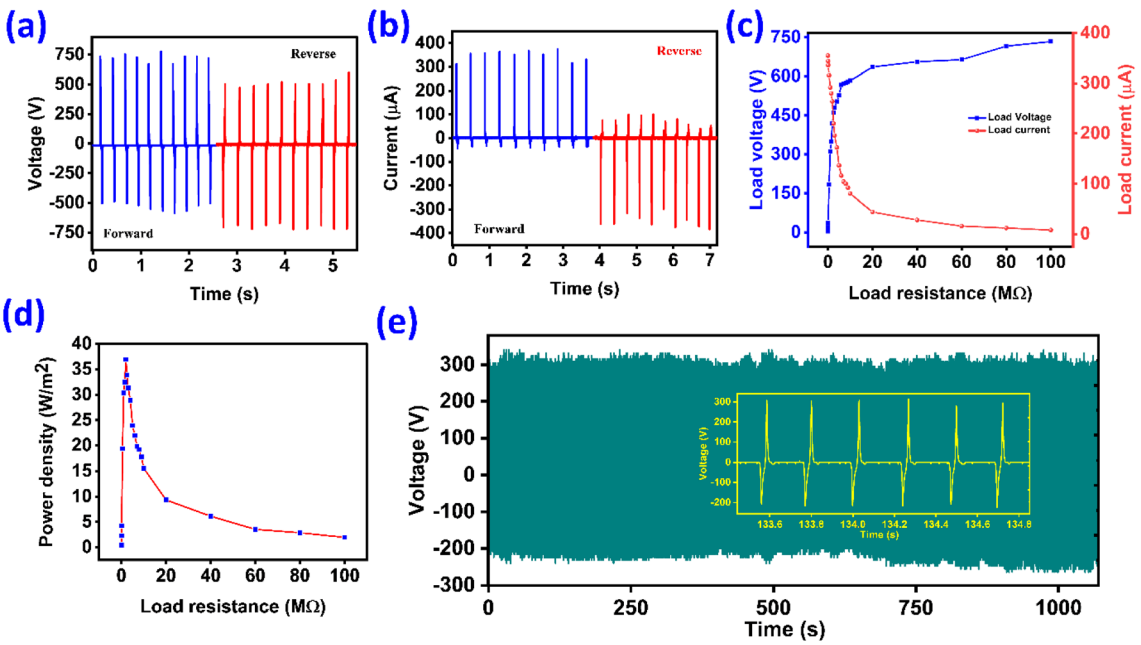

Fig. 5 (a) and (b) V_{oc} and I_{sc} response of the TENG in forward and reverse connections, (c) variation of voltage and current of the TENGs under different load resistance values, (d) instantaneous power density of the TENGs with load resistance, (e) stability of the TENG under ~5200 cycles (inset magnified view of a few cycles).

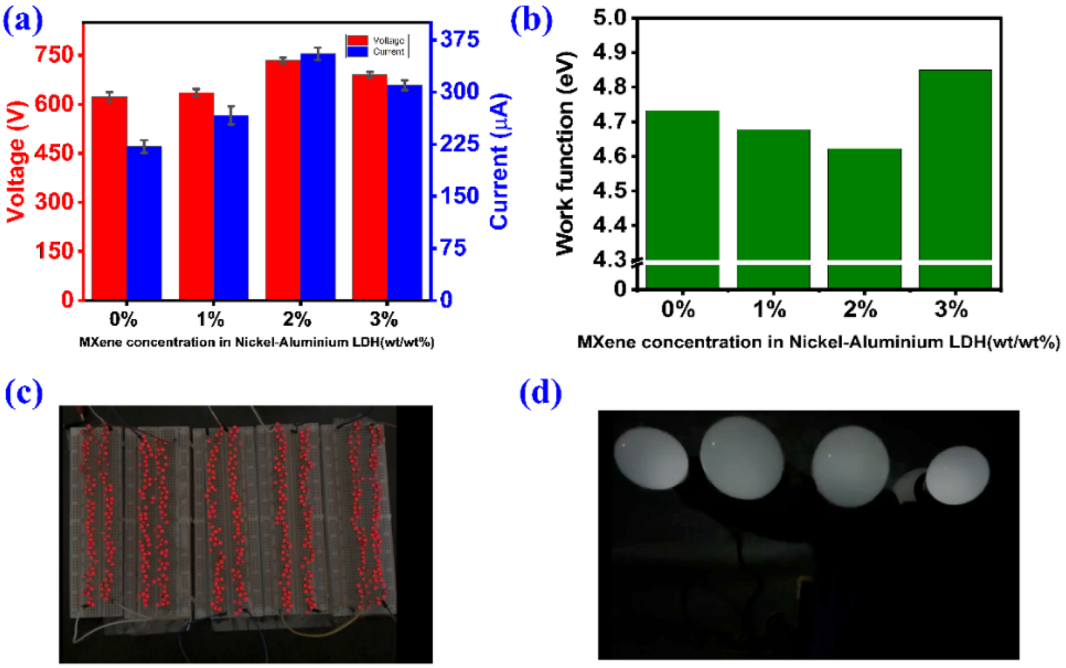

Fig. 6 (a) Output performance of the TENG at different MXene concentrations, (b) work function of NiAl-LDH at different MXene concentrations, powering (c) LEDs and (d) LED lamps.

exhibited an output voltage of approximately 624 V and a current of 222 μA. As the MXene concentration increased, a significant improvement in the TENG's performance was observed. At 2% MXene concentration, the TENG achieved its peak performance, delivering an impressive output voltage of 731 V and a current of 355 μA. This enhancement can be attributed to the synergistic effect between the NiAl-LDH layers and the conductive MXene, which facilitates efficient charge transfer and increases surface charge density. The interconnected network of uniformly distributed LDH on conductive MXene enhances the contact surface area and active sites, promoting efficient electron transfer between the triboelectric layers. However, further increasing the MXene concentration to 3% resulted in a decline in performance, with the output voltage dropping to 690 V and the current to 310 μA. The observed decrease in TENG performance at higher MXene concentrations can be attributed to the intrinsic electronegative nature of MXene, which diminishes the electron-donating capability of the NiAl-LDH/MXene composite. MXene enhances the charge transfer process at optimal concentrations by increasing conductivity and facilitating electrostatic interactions. However, as the concentration of MXene exceeds the optimal level, its strong electronegativity starts to dominate, reducing the effective triboelectric charge generation. This behaviour likely stems from an imbalance in the electron-donation and electron-acceptance processes within the composite. The excessive MXene content may also disrupt the uniformity and surface interaction of the composite, further limiting the ability of the TENG to generate and transfer charges effectively. These findings highlight the importance of fine-tuning the MXene concentration to maintain an ideal balance between enhancing conductivity and preserving the triboelectric properties of the composite.

This assumption was further validated by measuring the work function of each MXene concentration sample using ultraviolet photoelectron spectroscopy (UPS) (ESI S8†). The work function values for 0%, 1%, 2%, and 3% MXene concentrations are presented in Fig. 6(b).[47] For pure NiAl-LDH (0% MXene), the work function was found to be 4.73 eV. As the MXene concentration increased, the work function decreased, reaching its minimum value of 4.62 eV at 2% MXene concentration. This reduction in work function correlates directly with the enhanced performance of the TENG, as the lowest work function at 2% MXene concentration facilitates improved charge transfer efficiency, resulting in the highest output voltage and current. However, when the MXene concentration was increased further to 3%, the work function rose to 4.85 eV. This increase in work function is likely due to the over-dominance of the electronegative MXene component, which alters the electron affinity of the composite, thereby diminishing its charge-donating capabilities. Consequently, the TENG output performance decreased, supporting the notion that the variation in the work function of the composite plays a critical role in determining the device's output performance. This analysis underscores the importance of optimizing the MXene concentration to achieve a balanced electronic structure for maximum triboelectric performance.

The high output power TENG was utilized to power up 600 LEDs and four LED lamps momentarily for each hand tapping. The real-time demonstration is presented in ESI Videos V1 and V2.† Fig. 6(c) and (d) shows the photographs of the LEDs and LED lamps powered with TENG output.

3.3 Self-powered electroplating system

A self-powered electroplating setup was designed utilizing a fabricated TENG with a power management circuit (PMC), as shown in Fig. 7(a) and (b). In the present report, self-powered electroplating was performed using the simple bio-mechanical energy of hand tapping. The generated electricity was then fed into a PMC, which played a crucial role in regulating, storing, and delivering the energy in a controlled manner suitable for electroplating applications. The power management circuit included components such as rectifiers, capacitors, and inductors to ensure a steady and continuous power supply. The intermittent and variable nature of the TENG output was smoothed out by this circuit, storing the energy in capacitors or batteries for consistent use. The regulated power was then directed to the electroplating cell, where it facilitated the deposition of metal ions onto a conductive substrate, forming a uniform and adherent metal coating. By eliminating the need for an external power source, this setup reduced operational costs, enhanced energy efficiency and promoted sustainability by utilizing renewable mechanical energy. Moreover, the self-powered nature of this system made it highly versatile and portable, enabling its application in remote or off-grid locations.

By leveraging the unidirectional output and impedance-matching properties of the TENG, the PMC ensures that energy harvested by the TENG is effectively stored in a capacitor through a two-stage energy transfer mechanism.[48] In the first stage, the electrical energy from the TENG is converted into magnetic energy stored in the inductor (10 mH). This magnetic energy is then transformed back into electrical energy during the second stage and stored in the capacitor (10 μF). This cyclical process ensures minimal energy loss and maximizes storage efficiency. The integration of TENGs with PMC was seen to hold great promise for revolutionizing electroplating processes, making them more eco-friendly and adaptable to various industrial needs. This method produces high-quality copper coatings suitable for applications in electronics, jewellery, and industrial components.

The process involved preparing an electrolyte solution containing copper sulfate ($CuSO_4$) and sulfuric acid (H_2SO_4) to supply Cu^{2+} ions, as shown in Fig. 7(c). The TENG device was connected to the electroplating circuit, with the iron substrate as the cathode and a pure copper strip as the anode. During the process, copper atoms at the anode were oxidized to Cu^{2+} ions, which were then reduced at the cathode, resulting in the deposition of a copper layer onto the iron surface. The reactions at anode and cathode are

$$\text{Cathode: } Cu_{(aq)}^{2+} + 2e^- \rightarrow Cu_{(s)} \quad (1)$$

$$\text{Anode: } Cu_{(s)} \rightarrow Cu_{(aq)}^{2+} + 2e^- \quad (2)$$

The continuous electrical energy generated by the TENG facilitated the gradual formation of a uniform copper coating on the iron sheet, which was subsequently rinsed and dried to complete the plating process. The real-time demonstration of self-powered electroplating is included in the ESI in Videos V3 and V4.† Fig. 7(d) shows the photographs of the iron sheets before and after electroplating with the TENG for a period of

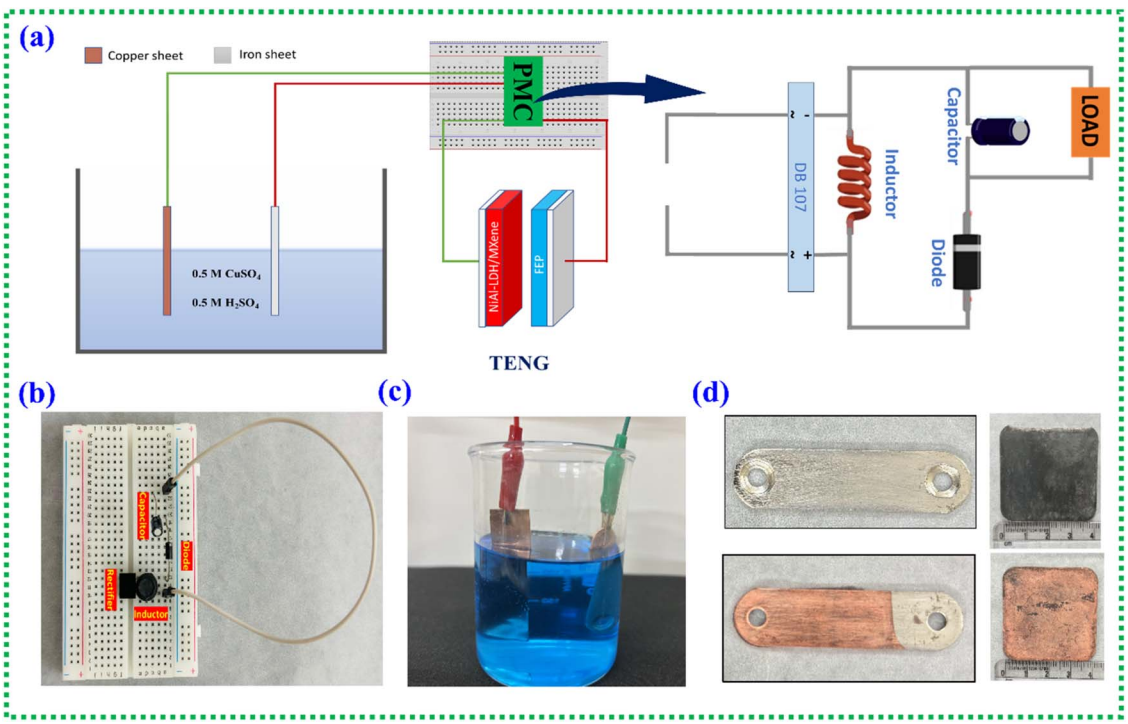

Fig. 7 (a) Schematic of the self-powered copper plating setup with a power management circuit, (b) images of the power management circuit, (c) reaction beaker with copper and iron metal sheet, (d) photographs of the copper plated pieces before and after electroplating.

~30 seconds. It was found that the proposed setup could achieve copper plating at a rate of 0.0004 g min^{-1} cm^2 and the details are provided in ESI S9.† To validate the role of the TENG in the electroplating process, an identical electroplating experiment was conducted with and without the application of TENG output to the electroplating setup over the same duration. It was found that no visible coating appeared on the metal in the absence of TENG input during the electroplating step. In contrast, the presence of TENG input in the electroplating process produced a clear, visible coating on the metal piece. The real-time demonstration of the electroplating process with and without the TENG is available in ESI Video. V5.†

In the proposed system, the TENG can be incorporated as a sustainable power source to extract energy from mechanical motions, eliminating the need for external electricity during the electroplating process. To validate the scalability and practicality of the system, we performed electroplating on metal substrates of various sizes (4×4 cm^2 and 7.5×7.5 cm^2) and shapes, confirming its practical applicability (ESI S10†). Furthermore, the system offers potential for large-scale deployment and integration of TENG-based self-powered systems into industrial metal finishing applications. For example, the current 5×5 cm^2 triboelectric layer can be expanded by employing scalable coating techniques such as spray coating or doctor blading to uniformly deposit the composite on larger substrates, enabling the creation of large-area TENGs. Additionally, modular TENG arrays can be designed by connecting multiple large-area TENG units in parallel, thereby increasing the overall power output to meet the energy demands of industrial electroplating systems. In the electroplating industry, large-area TENGs can power processes for coating metals in electronics, jewelry, and automotive components, reducing reliance on external power sources and lowering operational costs. The TENG's ability to harvest biomechanical or vibrational energy makes it suitable for integration into factory environments, where machinery vibrations can drive the TENG to power small-scale electrochemical systems. Another approach is to integrate large-area TENG devices into floor tiles, presenting an innovative way to harvest energy from walking to drive the electroplating system. Each step on and off the tiles would induce contact-separation cycles, producing electrical energy that can be stored *via* a power management circuit (PMC) and used to power the electroplating setup, similar to the hand-tapping method in our study.

4 Conclusion

A NiAl-LDH/MXene nanocomposite-based triboelectric nanogenerator (TENG) was successfully fabricated, demonstrating its potential for self-powered electroplating systems. The nanocomposite was prepared by successfully growing NiAl-LDH on MXene nanosheets, ensuring strong interfacial interactions and enhanced triboelectric properties. Among various tested triboelectric pairs, FEP exhibited the best compatibility with the nanocomposite, achieving the highest performance. The optimized TENG produced an impressive output with an open-circuit voltage of 734 V, a short-circuit current of 355 μA, and a power density of 36.9 W m^{-2}. Performance optimization was achieved by varying the concentration of MXene in the LDH matrix, where the enhancement was attributed to changes in the work function of the composite. Additionally, the fabricated TENG successfully powered a self-powered electroplating setup, demonstrating its practical applicability in real-world scenarios. This study highlights the significant potential of NiAl-LDH/MXene-based TENGs for next-generation energy harvesting and self-powered systems. Future work could explore the scalability and integration into various applications for sustainable energy solutions, as well as the relationship between electroplating processes and the performance of triboelectric devices.

Data availability

The data supporting this article have been included as part of the ESI.†

Author contributions

Navaneeth Madathil: data curation, formal analysis, investigation, methodology, validation, visualization, writing – original draft, writing – review & editing; Anjaly Babu: data curation, investigation, resources, visualization; Mahesh Velupula: data curation, investigation, resources, visualization; Anu Kulandaivel: data curation, investigation, resources, visualization; Rakesh Kumar Rajaboina: conceptualization, formal analysis, methodology, project administration, supervision, writing – original draft, writing – review & editing; Uday Kumar Khanapuram: formal analysis, project administration, validation, writing – original draft, writing – review & editing; Kamakshaiah Charyulu Devarayapalli: formal analysis, investigation, methodology, project administration, validation; Dae Sung Lee: conceptualization, formal analysis, supervision, writing – review & editing.

Conflicts of interest

The authors declare that they have no known competing financial interests or personal relationships that could have appeared to influence the work reported in this paper.

Acknowledgements

The authors would like to thank the Department of Physics and Centre for Research and Instrument Facility (CRIF), NIT Warangal, for providing their research facilities. This research was supported by the Basic Science Research Program through the National Research Foundation of Korea (NRF), funded by the Ministry of Education (NRF-2018R1A6A1A03024962).

References

1 P. Bai, G. Zhu, Z.-H. Lin, Q. Jing, J. Chen, G. Zhang, J. Ma and Z. L. Wang, Integrated Multilayered Triboelectric Nanogenerator for Harvesting Biomechanical Energy from

Human Motions, *ACS Nano*, 2013, **7**, 3713–3719, DOI: 10.1021/nn4007708.

2 J. Yang, J. Chen, Y. Yang, H. Zhang, W. Yang, P. Bai, Y. Su and Z. L. Wang, Broadband Vibrational Energy Harvesting Based on a Triboelectric Nanogenerator, *Adv. Energy Mater.*, 2014, **4**, 1301322, DOI: 10.1002/aenm.201301322.

3 B. Chen, Y. Yang and Z. L. Wang, Scavenging Wind Energy by Triboelectric Nanogenerators, *Adv. Energy Mater.*, 2018, **8**, 1702649, DOI: 10.1002/aenm.201702649.

4 Z. L. Wang, Triboelectric Nanogenerators as New Energy Technology for Self-Powered Systems and as Active Mechanical and Chemical Sensors, *ACS Nano*, 2013, **7**, 9533–9557, DOI: 10.1021/nn404614z.

5 R. D. I. G. Dharmasena, K. D. G. I. Jayawardena, C. A. Mills, J. H. B. Deane, J. V. Anguita, R. A. Dorey and S. R. P. Silva, Triboelectric nanogenerators: providing a fundamental framework, *Energy Environ. Sci.*, 2017, **10**, 1801–1811, DOI: 10.1039/C7EE01139C.

6 C. Wu, A. C. Wang, W. Ding, H. Guo and Z. L. Wang, Triboelectric Nanogenerator: A Foundation of the Energy for the New Era, *Adv. Energy Mater.*, 2019, **9**, 1–25, DOI: 10.1002/aenm.201802906.

7 A. A. Mathew, A. Chandrasekhar and S. Vivekanandan, A review on real-time implantable and wearable health monitoring sensors based on triboelectric nanogenerator approach, *Nano Energy*, 2021, **80**, 105566, DOI: 10.1016/j.nanoen.2020.105566.

8 R. Zhang and H. Olin, Material choices for triboelectric nanogenerators: A critical review, *EcoMat*, 2020, **2**, e12012, DOI: 10.1002/eom2.12062.

9 A. Kulandaivel, S. Potu, A. Babu, N. Madathil, M. Velpula, R. K. Rajaboina and U. K. Khanapuram, Advances in ferrofluid-based triboelectric nanogenerators: Design, performance, and prospects for energy harvesting applications, *Nano Energy*, 2024, **120**, 109110, DOI: 10.1016/j.nanoen.2023.109110.

10 F. R. Fan, Z. Q. Tian and Z. L. Wang, Flexible triboelectric generator, *Nano Energy*, 2012, **1**, 328–334, DOI: 10.1016/j.nanoen.2012.01.004.

11 F.-R. Fan, L. Lin, G. Zhu, W. Wu, R. Zhang and Z. L. Wang, Transparent Triboelectric Nanogenerators and Self-Powered Pressure Sensors Based on Micropatterned Plastic Films, *Nano Lett.*, 2012, **12**, 3109–3114, DOI: 10.1021/nl300988z.

12 S. Potu, A. Kulandaivel, B. Gollapelli, U. K. Khanapuram and R. K. Rajaboina, Oxide based triboelectric nanogenerators: recent advances and future prospects in energy harvesting, *Mater. Sci. Eng., R*, 2024, **161**, 100866, DOI: 10.1016/j.mser.2024.100866.

13 B. Baro, S. Khimhun, U. Das and S. Bayan, ZnO based triboelectric nanogenerator on textile platform for wearable sweat sensing application, *Nano Energy*, 2023, **108**, 108212, DOI: 10.1016/j.nanoen.2023.108212.

14 T. Charoonsuk, S. Pongampai, P. Pakawanit and N. Vittayakorn, Achieving a highly efficient chitosan-based triboelectric nanogenerator *via* adding organic proteins: influence of morphology and molecular structure, *Nano Energy*, 2021, **89**, 106430, DOI: 10.1016/j.nanoen.2021.106430.

15 H.-J. Kim, E.-C. Yim, J.-H. Kim, S.-J. Kim, J.-Y. Park and I.-K. Oh, Bacterial Nano-Cellulose Triboelectric Nanogenerator, *Nano Energy*, 2017, **33**, 130–137, DOI: 10.1016/j.nanoen.2017.01.035.

16 K. U. Kumar, S. Hajra, G. Mohana Rani, S. Panda, R. Umapathi, S. Venkateswarlu, H. J. Kim, Y. K. Mishra and R. R. Kumar, Revolutionizing waste-to-energy: harnessing the power of triboelectric nanogenerators, *Adv. Compos. Hybrid Mater.*, 2024, **7**, 91, DOI: 10.1007/s42114-024-00903-9.

17 B. Dudem, R. D. I. G. Dharmasena, R. Riaz, V. Vivekananthan, K. G. U. Wijayantha, P. Lugli, L. Petti and S. R. P. Silva, Wearable Triboelectric Nanogenerator from Waste Materials for Autonomous Information Transmission *via* Morse Code, *ACS Appl. Mater. Interfaces*, 2022, **14**, 5328–5337, DOI: 10.1021/acsami.1c20984.

18 S.-J. Park, M.-L. Seol, D. Kim, S.-B. Jeon and Y.-K. Choi, Triboelectric nanogenerator with nanostructured metal surface using water-assisted oxidation, *Nano Energy*, 2016, **21**, 258–264, DOI: 10.1016/j.nanoen.2016.01.021.

19 B. Xu, W. Peng, J. He, Y. Zhang, X. Song, J. Li, Z. Zhang, Y. Luo, X. Meng, C. Cai, Y. Liu, Z. Wei, S. Wang, S. Nie and Q. Duan, Liquid metal-based triboelectric nanogenerators for energy harvesting and emerging applications, *Nano Energy*, 2024, **120**, 109107, DOI: 10.1016/j.nanoen.2023.109107.

20 S. Ghorbanzadeh and W. Zhang, Advances in MXene-based triboelectric nanogenerators, *Nano Energy*, 2024, **125**, 109558, DOI: 10.1016/j.nanoen.2024.109558.

21 Y. Dong, S. S. K. Mallineni, K. Maleski, H. Behlow, V. N. Mochalin, A. M. Rao, Y. Gogotsi and R. Podila, Metallic MXenes: A new family of materials for flexible triboelectric nanogenerators, *Nano Energy*, 2018, **44**, 103–110, DOI: 10.1016/j.nanoen.2017.11.044.

22 G. Khandelwal, A. Chandrasekhar, N. P. Maria Joseph Raj and S. Kim, Metal–Organic Framework: A Novel Material for Triboelectric Nanogenerator–Based Self-Powered Sensors and Systems, *Adv. Energy Mater.*, 2019, **9**, 1803581, DOI: 10.1002/aenm.201803581.

23 R. K. Rajaboina, U. K. Khanapuram, V. Vivekananthan, G. Khandelwal, S. Potu, A. Babu, N. Madathil, M. Velpula and P. Kodali, Crystalline Porous Material-Based Nanogenerators: Recent Progress, Applications, Challenges, and Opportunities, *Small*, 2024, **20**, 2306209, DOI: 10.1002/smll.202306209.

24 J. Gao, B. Jin and M. Shao, Layered double hydroxides functionalization toward rechargeable batteries, *Particuology*, 2024, **91**, 138–154, DOI: 10.1016/j.partic.2024.02.003.

25 L. Li, I. Soyhan, E. Warszawik and P. van Rijn, Layered Double Hydroxides: Recent Progress and Promising Perspectives Toward Biomedical Applications, *Adv. Sci.*, 2024, **11**, 2306035, DOI: 10.1002/advs.202306035.

26 J. Li, N. Zhao, X. Liu, X. Chang, W. Zheng and J. Zhang, Two-dimensional layered double hydroxides for advanced

sensors, *Coord. Chem. Rev.*, 2025, **523**, 216262, DOI: 10.1016/j.ccr.2024.216262.

27 S. Deng, W. Akram, X. Ye, L. Zhang, Y. Yang, S. Cheng and J. Fang, Comprehensive Insights on MXene-Based TENGs: from Structures, Functions to Applications, *Small*, 2024, 2404872, DOI: 10.1002/smll.202404872.

28 S. Ghorbanzadeh and W. Zhang, Advances in MXene-based triboelectric nanogenerators, *Nano Energy*, 2024, **125**, 109558, DOI: 10.1016/j.nanoen.2024.109558.

29 P. Das and Z.-S. Wu, MXene for energy storage: present status and future perspectives, *J. Phys.: Energy*, 2020, **2**, 032004, DOI: 10.1088/2515-7655/ab9b1d.

30 Y. Song, Z. Sun, P. Kong, H. Gui, Y. Li, Y. Wang, J. Tang and L. Huang, Recent advances in MXene based intelligent sensing, *Chem. Eng. J.*, 2024, **500**, 157305, DOI: 10.1016/j.cej.2024.157305.

31 Y. Zhou, Y. Zhang, K. Ruan, H. Guo, M. He, H. Qiu and J. Gu, MXene-based fibers: Preparation, applications, and prospects, *Sci. Bull.*, 2024, **69**, 2776–2792, DOI: 10.1016/j.scib.2024.07.009.

32 S. Venkateshalu, G. M. Tomboc, S. P. Nagalingam, J. Kim, T. Sawaira, K. Sehar, B. G. Pollet, J. Y. Kim, A. Nirmala Grace and K. Lee, Synergistic MXene/LDH heterostructures with extensive interfacing as emerging energy conversion and storage materials, *J. Mater. Chem. A*, 2023, **11**, 14469–14488, DOI: 10.1039/D3TA01992F.

33 Y. Wang, H. Dou, J. Wang, B. Ding, Y. Xu, Z. Chang and X. Hao, Three-dimensional porous MXene/layered double hydroxide composite for high performance supercapacitors, *J. Power Sources*, 2016, **327**, 221–228, DOI: 10.1016/j.jpowsour.2016.07.062.

34 A. Thakur, N. Chandran B.S., K. Davidson, A. Bedford, H. Fang, Y. Im, V. Kanduri, B. C. Wyatt, S. K. Nemani, V. Poliukhova, R. Kumar, Z. Fakhraai and B. Anasori, Step-by-Step Guide for Synthesis and Delamination of $Ti_3C_2T_x$MXene, *Small Methods*, 2023, **7**, 2300030, DOI: 10.1002/smtd.202300030.

35 S. Tonda and W.-K. Jo, Plasmonic Ag nanoparticles decorated NiAl-layered double hydroxide/graphitic carbon nitride nanocomposites for efficient visible-light-driven photocatalytic removal of aqueous organic pollutants, *Catal. Today*, 2018, **315**, 213–222, DOI: 10.1016/j.cattod.2017.12.019.

36 S. Zhao, D. Pan, Q. Liang, M. Zhou, C. Yao, S. Xu and Z. Li, Ultrathin NiAl-Layered Double Hydroxides Grown on 2D $Ti_3C_2T_x$MXene to Construct Core–Shell Heterostructures for Enhanced Photocatalytic CO_2 Reduction, *J. Phys. Chem. C*, 2021, **125**, 10207–10218, DOI: 10.1021/acs.jpcc.1c00017.

37 L. Wang, X. Chen, C. Liu and W. Yang, Non-enzymatic acetylcholine electrochemical biosensor based on flower-like NiAl layered double hydroxides decorated with carbon dots, *Sens. Actuators, B*, 2016, **233**, 199–205, DOI: 10.1016/j.snb.2016.04.062.

38 Z. Bian, H. Huang, Y. Ma, F. Guo, Y. Shang, Y. Zhang and J. Xu, NiAl-Layer double hydroxide loading on MXenes nanosheets with boehmite-assisted for improved electrochemical performance, *Ionics*, 2023, **29**, 2365–2376, DOI: 10.1007/s11581-023-04987-z.

39 Y. Wang, H. Dou, J. Wang, B. Ding, Y. Xu, Z. Chang and X. Hao, Three-dimensional porous MXene/layered double hydroxide composite for high performance supercapacitors, *J. Power Sources*, 2016, **327**, 221–228, DOI: 10.1016/j.jpowsour.2016.07.062.

40 H. Dong, X. Zhang, Y. Zuo, N. Song, X. Xin, B. Zheng, J. Sun, G. Chen and C. Li, 2D Ti3C2 as electron harvester anchors on 2D g-C3N4 to create boundary edge active sites for boosting photocatalytic performance, *Appl. Catal., A*, 2020, **590**, 117367, DOI: 10.1016/j.apcata.2019.117367.

41 Y. Wang, X. Gao, L. Zhang, X. Wu, Q. Wang, C. Luo and G. Wu, Synthesis of Ti3C2/Fe3O4/PANI hierarchical architecture composite as an efficient wide-band electromagnetic absorber, *Appl. Surf. Sci.*, 2019, **480**, 830–838, DOI: 10.1016/j.apsusc.2019.03.049.

42 D. S. Abraham, M. Chandran, M. Vinoba, R. Yamuna and M. Bhagiyalakshmi, Flower-like Layered NiCu-LDH/MXene Nanocomposites as an Anodic Material for Electrocatalytic Oxidation of Methanol, *Langmuir*, 2023, **39**, 4756–4765, DOI: 10.1021/acs.langmuir.3c00154.

43 J. Guo, Z. Bian, L. Ye, Y. Shang, F. Guo, Y. Zhang and J. Xu, Double layers combined with MXene and *in situ* grown NiAl-LDH arrays on nickel foam for enhanced asymmetric supercapacitors, *Ionics*, 2022, **28**, 2967–2977, DOI: 10.1007/s11581-022-04520-8.

44 S. Niu, S. Wang, L. Lin, Y. Liu, Y. S. Zhou, Y. Hu and Z. L. Wang, Theoretical study of contact-mode triboelectric nanogenerators as an effective power source, *Energy Environ. Sci.*, 2013, **6**, 3576–3583, DOI: 10.1039/C3EE42571A.

45 J. Xiong, P. Cui, X. Chen, J. Wang, K. Parida, M.-F. Lin and P. S. Lee, Skin-touch-actuated textile-based triboelectric nanogenerator with black phosphorus for durable biomechanical energy harvesting, *Nat. Commun.*, 2018, **9**, 4280, DOI: 10.1038/s41467-018-06759-0.

46 M. Navaneeth, S. Potu, A. Babu, B. Lakshakoti, R. K. Rajaboina, U. Kumar K, H. Divi, P. Kodali and K. Balaji, Transforming Medical Plastic Waste into High-Performance Triboelectric Nanogenerators for Sustainable Energy, Health Monitoring, and Sensing Applications, *ACS Sustain. Chem. Eng.*, 2023, **11**, 12145–12154, DOI: 10.1021/acssuschemeng.3c03136.

47 Z. L. Wang and A. C. Wang, On the origin of contact-electrification, *Mater. Today*, 2019, **30**, 34–51, DOI: 10.1016/j.mattod.2019.05.016.

48 H. Qin, G. Cheng, Y. Zi, G. Gu, B. Zhang, W. Shang, F. Yang, J. Yang, Z. Du and Z. L. Wang, High Energy Storage Efficiency Triboelectric Nanogenerators with Unidirectional Switches and Passive Power Management Circuits, *Adv. Funct. Mater.*, 2018, **28**, 1805216, DOI: 10.1002/adfm.201805216.

